

# $\beta$ -Variational autoencoders and transformers for reduced-order modelling of fluid flows

Alberto Solera-Rico<sup>1,2</sup>, Carlos Sanmiguel Vila<sup>1,2</sup>, M. Á. Gómez<sup>2</sup>, Yuning Wang<sup>4</sup>, Abdulrahman Almashjary<sup>3</sup>, Scott T. M. Dawson<sup>3</sup>, Ricardo Vinuesa<sup>4</sup>

1: *Aerospace Engineering Research Group, Universidad Carlos III de Madrid, Leganés, Spain*

2: *Subdirectorate General of Terrestrial Systems,*

*Spanish National Institute for Aerospace Technology (INTA), San Martín de la Vega, Spain*

3: *Mechanical, Materials, and Aerospace Engineering Department,*

*Illinois Institute of Technology, Chicago, IL 60616*

4: *FLOW, Engineering Mechanics, KTH Royal Institute of Technology, SE-100 44 Stockholm, Sweden*

Variational autoencoder (VAE) architectures have the potential to develop reduced-order models (ROMs) for chaotic fluid flows. We propose a method for learning compact and near-orthogonal ROMs using a combination of a  $\beta$ -VAE and a transformer, tested on numerical data from a two-dimensional viscous flow in both periodic and chaotic regimes. The  $\beta$ -VAE is trained to learn a compact latent representation of the flow velocity, and the transformer is trained to predict the temporal dynamics in latent space. Using the  $\beta$ -VAE to learn disentangled representations in latent-space, we obtain a more interpretable flow model with features that resemble those observed in the proper orthogonal decomposition, but with a more efficient representation. Using Poincaré maps, the results show that our method can capture the underlying dynamics of the flow outperforming other prediction models. The proposed method has potential applications in other fields such as weather forecasting, structural dynamics or biomedical engineering.

## Introduction

Turbulent flows are an important and ubiquitous phenomenon in nature and engineering, with applications ranging from aircraft design to weather forecasting. Understanding the behaviour of fluid flows is often challenging due to their complex spatio-temporal dynamics involving a large number of degrees of freedom and complex non-linear interactions [1]. As a result, there is a growing interest in developing reduced-order models (ROMs) of fluid flow dynamics that can capture the key underlying dynamics of the flow while reducing the problem dimensionality [2, 3]. Developing ROMs is one of the most prominent research fields since they facilitate finding low-dimensional representations that can be applied to perform flow control applications [4] or reduce the computational cost of numerical simulations [5, 6]. One of the most used techniques for dimensionality reduction in the fluid-dynamics community is proper orthogonal decomposition (POD), which involves finding the dominant modes of variation in a given dataset and projecting the data onto a lower-dimensional subspace spanned by these modes. Another famous linear approach is the dynamic-mode decomposition (DMD), which identifies dynamic modes that govern the evolution of the system over time [7]. While POD and DMD, as well as the extensions of these methods such as the spectral POD [8] or the higher-order DMD [9], have successfully reduced the dimensionality of some flows [10], their optimal linear bases exhibit limitations when working with turbulent flows, which typically involve complex non-linear interactions [11].

In recent years, machine-learning (ML) techniques have emerged as promising approaches for developing ROMs of fluid-flow dynamics [6, 12–16]. One of the potential ML techniques adopted to create non-linear ROMs is the neural networks with convolutional autoencoder architectures. These architectures comprise of both an encoder and a decoder trained to minimize the reconstruction error between the encoded-decoded data and the initial data. The resulting encoder allows obtaining a latent-space composed of non-linear representations. Then, neural-network architectures suitable for temporal predictions [12, 17], such as long short-term memory (LSTM) networks, can be used to model the dynamics of the non-linear latent-space, resulting in a fast surrogate model for fluid-flow predictions.

Among the different autoencoder architectures, variational autoencoders (VAEs) have proven to be effective for encoding the spatial information of fluid flows in non-linear low-dimensional latent-spaces [12]. Unlike a standard autoencoder, a VAE architecture is based on a probabilistic framework for describing an observation in latent-space by including an additional loss term on the latent-space variables. However, the low-dimensional representations obtained using these architectures lack the orthogonality of the classical linear-decomposition techniques. To overcome this issue, the  $\beta$ -VAE architecture introduced in Refs. [18, 19] modifies the loss function of the VAE by adding a regularisation parameter to balance the reconstruction accuracy with regularisation and mode disentanglement. The potential of these architectures to develop a compact and near-orthogonal ROM was reported in Ref. [20], where they tested this architecture in a high-fidelity simulation of a turbulent flow through a simplified urban environment. The results showed a ROM that was able to capture up to 87.36% of the original energy with only five modes, compared to the 32.41% obtained with five POD modes.

For the temporal predictions, the LSTM has been shown to be an effective architecture in turbulent flows [17, 21, 22].

However, in the latest years, another neural-network architecture known as transformer [23] appears to have the potential to outperform the LSTM and allow the development of more complex ROMs. The transformer is a deep neural-network architecture that has gained widespread attention in recent years due to their state-of-the-art performance in natural-language-processing (NLP) tasks such as language translation [24] or text generation [25]. Unlike traditional recurrent neural networks like LSTM, which process sequential data one element at a time, transformers are designed to capture long-range dependencies between elements in a sequence. This capability is achieved using self-attention mechanisms which allow the network to attend to different parts of the input sequence at each network layer. As a result, transformers have been shown to outperform previous state-of-the-art methods in several NLP benchmarks, often by large margins.

The success of transformers in NLP has led to their application in other domains, including computer vision [26, 27], audio processing [28], and robotics [29]. In particular, due to their ability to capture long-range dependencies, transformers are particularly well suited to model dynamic systems [30]. In fact, transformers are able to represent the multi-scale character of turbulence in long temporal sequences [31]; this can only be captured by LSTMs when separately predicting modes of different ranges of frequencies [32]. In these applications, the goal is to learn a low-dimensional representation of the system that captures the underlying dynamics, which can then be used to make predictions or generate new trajectories. Transformers are a promising tool for this task, as they can learn complex temporal dependencies and capture long-term trends in the data while allowing efficient parallel processing.

The potential combination of autoencoder architectures, which enable obtaining near-orthogonal non-linear latent-spaces, with transformer architectures for the dynamics of the temporal predictions, is a powerful tool that can be employed to model complex flows with a higher level of accuracy. For this reason, in this paper, we propose a  $\beta$ -VAE and transformer-based model for encoding the fluid-flow velocity fields and learning a ROM of its spatio-temporal dynamics. Two flow cases are analysed, namely a periodic and a chaotic configuration of a two-dimensional, viscous flow over two collinear flat plates, obtained by numerical simulation. Flow past multiple bodies in close configuration is relevant for a range of applications, such as buildings or chimneys in urban and industrial environments, power lines, offshore structures, and heat exchangers. Even at relatively low Reynolds numbers, such flows can exhibit substantially more complexity than flow over a single, isolated body [33–35].

The resulting latent-space of  $\beta$ -VAEs is analysed using POD as a reference case to analyse the resulting spatial mode features, and different latent-spaces are tested. The temporal predictions of the latent-space dynamics performed using transformer-based architectures are compared with other ML temporal models, including LSTMs and Koopman with Non-linear Forcing [36]. Finally, the predictions are assessed using the reconstructed predicted fields and Poincaré maps to assess the dynamic behaviour of the resulting ROMs.

## Results

We compare the behaviour of  $\beta$ -VAE and POD as defined in Methods using the following metrics to compare their energy reconstruction and orthogonality performance.

For the  $\beta$ -VAE, following Ref. [20], the energy percentage  $E_k$  that is captured by the model reconstructions is defined as:

$$E_k = \left( 1 - \left\langle \frac{\sum_{i=1}^{N_p} \sum_{j=1}^2 (u_j - \tilde{u}_j)^2}{\sum_{i=1}^{N_p} \sum_{j=1}^2 u_j^2} \right\rangle \right) \times 100, \quad (1)$$

where  $\langle \cdot \rangle$  indicates ensemble averaging in time,  $N_p$  is the number grid points along the spatial domain  $u_j$  denotes the  $j^{th}$  reference value of fluctuating component velocity and  $\tilde{u}_j$  its reconstruction, respectively. To measure the orthogonality of the latent variables, we compute the determinant of the correlation matrix multiplied by 100 and refer to it as  $\det_{\mathbf{R}}$ , where  $\mathbf{R} = (\mathbf{R})_{d \times d}$  is the correlation matrix defined by:

$$R_{ii} = 1, \quad R_{ij} = \frac{C_{ij}}{\sqrt{C_{ii}C_{jj}}}, \quad (2)$$

for all  $1 \leq i \neq j \leq d$  where  $C_{ij}$  denotes the components  $i, j$  of the covariance matrix  $\mathbf{C}$  and  $d$  is the dimension of the latent-space. A value of 1 is reached when all the variables are completely uncorrelated ( $R_{ij} = 0$ ) and zero when they are completely correlated ( $R_{ij} = 1$ ), this metric is used to report the independence of the latent variables.

For the POD, the modes are orthogonal by definition and the energy percentage captured by the POD reconstruction is determined using the cumulative energy recovery defined as:

$$E_k = \frac{\sum_{i=1}^{N_m} \lambda_i}{\sum_i \lambda_i} \times 100, \quad (3)$$

where  $\lambda_i$  are the eigenvalues representative of the energy contribution of each mode.

The modes have been ordered according to their cumulative contribution to the reconstructed energy,  $E_k$ , following Ref. [20]. The first mode is chosen as the one with the largest individual contribution to  $E_k$ , and the next are those that have the maximum contribution when added to the previous modes.

### Analysis of the latent-spaces

In this section, the  $\beta$ -VAE architecture and the POD are applied to two flow cases generated from a numerical simulation of a two-dimensional, viscous flow around two collinear flat plates. The characteristics of both cases are discussed next:

- Periodic flow with Reynolds number based on the freestream velocity  $U_\infty$  and (single-plate) chord length  $c$  of  $Re = 40$ , where the two collinear plates are arranged at an angle of  $90^\circ$  with respect to the incoming flow. Total of 1,000 instantaneous flow fields.
- Chaotic flow with Reynolds number of  $Re = 100$ , where the two collinear plates are arranged at an angle of  $80^\circ$  with respect to the incoming flow. Total of 9,095 instantaneous flow fields.

In both cases the domain where data is collected has dimensions  $96c \times 28c$ , where the spatial resolution is  $300 \times 98$  grid points with a uniform grid spacing and a convective time  $\Delta t = c/U_\infty = t_c$  separation between snapshots (downsampled in both space and time from the original simulations). A more detailed dataset description is given in the Methods section.

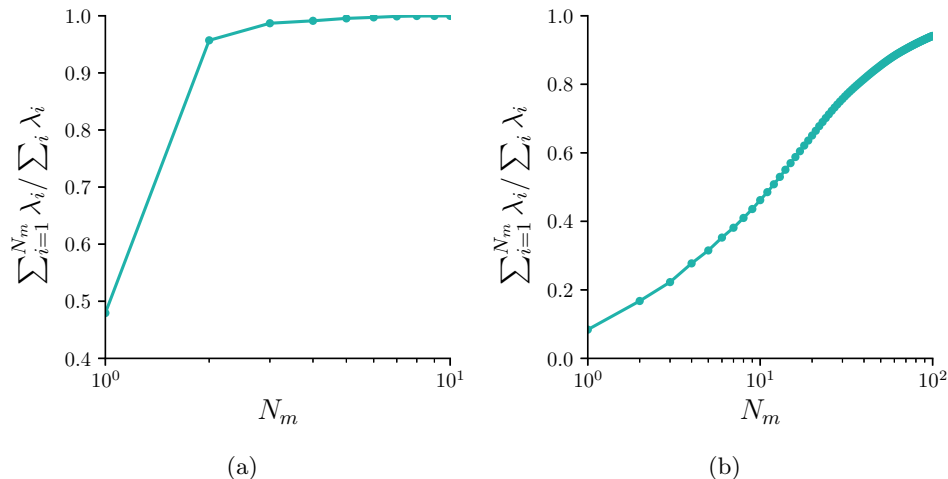


FIG. 1: Fraction of energy reconstructed by POD as a function of number of modes. (a)  $Re = 40$ ,  $\alpha = 90^\circ$ , (b)  $Re = 100$ ,  $\alpha = 80^\circ$ .

The periodic case is used as a benchmark to validate the physical soundness of the  $\beta$ -VAE model representations. This flow case can be adequately represented only using two POD modes that can represent  $E_k = 98.4\%$  of the kinetic energy of the fluctuations with respect to the base flow, as observed in Figure 1(a). In Figure 2, the first two rows show the two most energetic POD modes, which are identified as a shedding wake. For the  $\beta$ -VAE with  $\beta = 0.001$ , the results from the last two rows in Figure 2 show the spatial modes which, as explained previously, are obtained only using the decoder network with an input vector  $\mathbf{s}_i$  containing a unit value in the desired  $i^{th}$  position and zero elsewhere. The reconstructed energy in this case is equal to  $E_k = 99.4\%$  and  $\det_{\mathbf{R}} > 0.999$ . It is observed from Figure 2 that the spatial modes obtained from both methods exhibit the same pattern of shedding flow. The spectrum of the temporal coefficients for both methods is shown in the last column of Figure 2. The spectra analysis is from the resulting  $\mathbf{r}_i$  and  $\mathbf{a}_i$  time coefficients for the  $\beta$ -VAE and POD, respectively. This further confirms that the dynamics

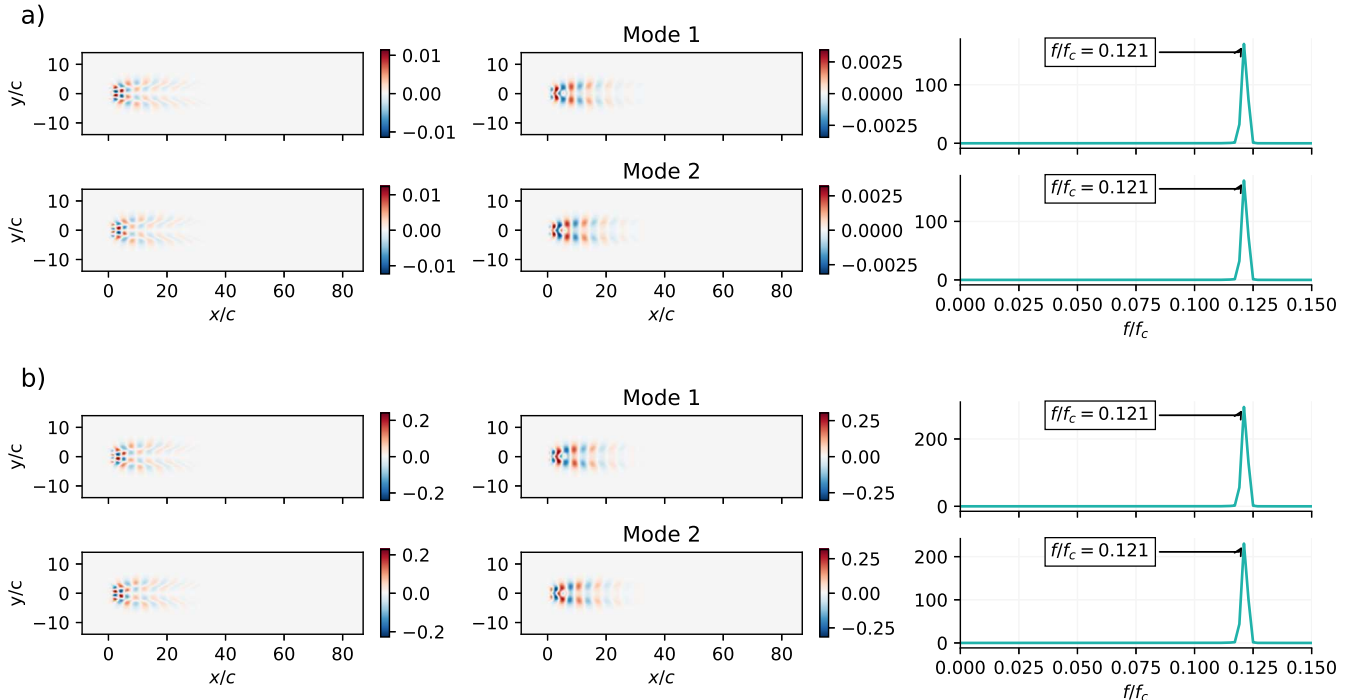


FIG. 2: Resulting modes for the  $Re = 40$ ,  $\alpha = 90$  case: a) POD, b)  $\beta$ -VAE. The first column contains the streamwise-velocity component modes sampled with a unit value, and the second one the crosswise-velocity component. The third column represents the frequency content in the temporal coefficient associated with each of the modes ( $f_c = U_\infty/c$ ); note that in b) this frequency content is evaluated in the latent-space.

associated with the spatial modes are also in good agreement: both methods can capture the same characteristic frequency. This result shows that the latent-space also exhibits meaningful physical phenomena of the flows.

Since the  $\beta$ -VAE architecture requires the user to set a latent-space dimension  $d$ , it can be argued that  $d$  can be set to a value larger than 2. However, we observed that models with larger latent-spaces produce only two meaningful modes, as the remaining modes have negligible values. This behaviour shows that the  $\beta$ -VAE regularisation effectively avoids the artificial creation of more modes than necessary to represent the solution. In the work by Eivazi *et al.* [20] it was shown that the  $\beta$ -VAE produces compact representations of latent-spaces, which suggests that these architectures may be a good framework in cases that can be represented with few energetic phenomena.

After this first assessment of the latent-spaces created by the  $\beta$ -VAE architectures, a non-linear and higher-dimensional chaotic case at  $Re = 100$  with the two collinear plates arranged at an angle of  $80^\circ$  with respect to the incoming flow is tested. As well as the higher Reynolds number, the change in angle adds additional complexity to the configuration as the geometry is no longer symmetric with respect to the freestream. In this case, the size of the latent-space is set to be as small as possible but large enough to allow the separation of different physical effects in the resulting modes. In this relatively complex case, it is expected to find more variety of effects in the fluid flow, requiring a more nuanced mapping to the low-dimensional latent-space, and an evident lack of performance of linear methods such as POD.

To define an appropriate  $\beta$  value, different values were tested between 0.001 and 0.05 and the  $\det_{\mathbf{R}}$  and  $E_k$  were calculated to evaluate the performance in both metrics with a fixed latent-space. The value of  $\beta$  is chosen high enough to produce a near-orthogonal latent-space representation but as small as possible to avoid increasing the reconstruction error. After this study, a  $\beta = 0.05$  is chosen, and an analysis of the appropriate latent-space is followed. For this analysis, the loss terms from the  $\beta$ -VAE are analysed during the training process as reported in Figure 3, with a particular interest in the Kullback–Leibler (KL) divergence loss. The figure shows that, as expected, the reconstruction loss is lower for the  $\beta$ -VAE model with larger latent-space  $d = 20$ , as more information is allowed to flow through the autoencoder bottleneck. The less constrained latent-space also allows for a lower KL divergence loss, meaning the latent-space distributions are closer to standard normal distributions. This lower KL loss also reflects the better ability of the model to produce disentangled representations in the latent-space. In this case,  $E_k = 98.0\%$  and  $\det_{\mathbf{R}} = 0.944$ , indicating both a good reconstruction capability and low mode correlation.

On the other hand, the model with a smaller latent-space  $d = 5$  converges to a relatively higher reconstruction loss.

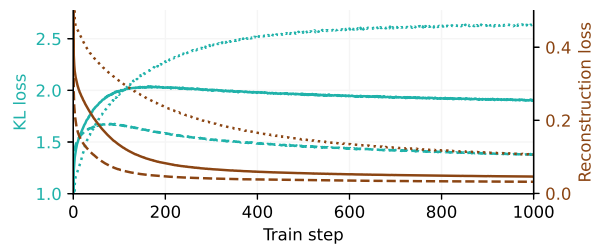


FIG. 3: Evolution of  $\beta$ -VAE losses during training: (dotted) 5 modes, (solid) 10 modes, (dashed) 20 modes. Losses are defined in the Methods section.

Even the KL loss term appears unable to converge during the training process because the bottleneck is too strict. For  $d = 5$ , the reconstructed energy  $E_k = 86.6\%$  and the determinant of the correlation matrix  $\det_{\mathbf{R}} = 0.993$ , reflect the loss of reconstruction capability due to the constrained bottleneck. The information is compressed into a few modes with less freedom for disentangled representation, a fact that implies that even for these architectures, a minimum number of modes is required to obtain an appropriate latent-space. The latent-space of size  $d = 10$  leads to a slight increase in reconstruction error compared to the model with  $d = 20$ , with an increased KL loss. However, in this case, the behaviour of the KL loss with a maximum and a later decay is indicative of the fact that the latent-space is sufficiently large to obtain convergence of the KL loss, and the gains in terms of reconstruction loss, in that case, are modest to justify a double number of modes. For these reasons, the  $\beta$ -VAE model with a latent-space of size  $d = 10$  was chosen as a reference for the present study. The values for the final model are  $E_k = 96.4\%$  and  $\det_{\mathbf{R}} = 0.982$ , indicating a good compromise between the reconstruction capability and the expected low correlation between modes.

Figure 4 shows, for each mode, the  $u$  and  $v$  components and the spectrum obtained from the temporal modes associated with each mode, while Figure 5 shows the same quantities obtained using POD. The spectral analysis of the temporal dynamics of the modes is used to identify different modes representing the same physical effect and provides helpful information for determining the size of the latent-space, since it allows more meaningful comparison with the POD. In this case, the  $\beta$ -VAE spatial modes are a non-linear combination of the most relevant flow features. Comparing the  $\beta$ -VAE and POD spectra, it can be seen that the  $\beta$ -VAE model can better separate different phenomena, each of which has its characteristic frequency associated with it, which appears as a peak in the spectrum. The different effects can be further isolated as individual modes by using larger latent-spaces. However, it is observed that the frequencies associated with the most energetic POD modes appear in the  $\beta$ -VAE dynamics, suggesting the idea that the  $\beta$ -VAE latent-spaces can find non-linear modes that effectively represent the dynamics of the system. The effect of the mode disentanglement produced by  $\beta$ -VAE models can be observed in the correlation matrix between the time series of each mode, Figure 6. As reported, the correlation between different modes of the time series is almost negligible due to the near-orthogonal representation in the latent-space. It is interesting to mention that, as in POD, for the case with  $d = 20$  analysing the temporal dynamics of the newly included modes more characteristic frequencies can be observed, which also appear in the range of the 10 to 20 POD modes. This result suggests that the latent-spaces created with these methods focus on obtaining the most energetic phenomena.

In POD orthogonality is ensured, being the mapping between physical and latent spaces linear. It is well known that chaotic flows often involve complex, non-linear interactions between fluid particles, which can lead to non-linear relationships between variables. As a result, the dominant modes of variability may not capture the complex, non-linear behaviour of the flow. This effect can be seen in Figure 7, where the first input to the  $\beta$ -VAE decoder network is sampled with different scalar values while the remaining inputs are kept to zero. The mode is sampled with input values in the range  $r_i \in [-2, 2]$  because during VAE training the latent-space is sampled from a near-standard normal distribution, driven by the KL-loss regularisation during training. The non-linear representation is evident as the shedding wake patterns change with the latent input value. This non-linear representation allows the  $\beta$ -VAE architecture to reproduce  $E_k = 96.42\%$  with only ten modes. In contrast, POD only yields  $E_k = 48.79\%$  and would require using over 100 modes to obtain a reconstruction above  $E_k = 95\%$ .

### Latent-space predictor models

In this section, the temporal dynamics of the latent-space  $\mathbf{r}_i$  for the case  $d = 10$  are combined with different ML models to implement a framework able to predict the temporal dynamics in the latent-space that can be used with the decoder from the  $\beta$ -VAE to obtain flow-field temporal predictions. With this purpose, a transformer model [23], a Koopman with Non-linear Forcing (KNF) model [36], and an LSTM network [37] are implemented and compared. The KNF and LSTM models have previously been analysed and compared in Ref. [22] and applied to predict the

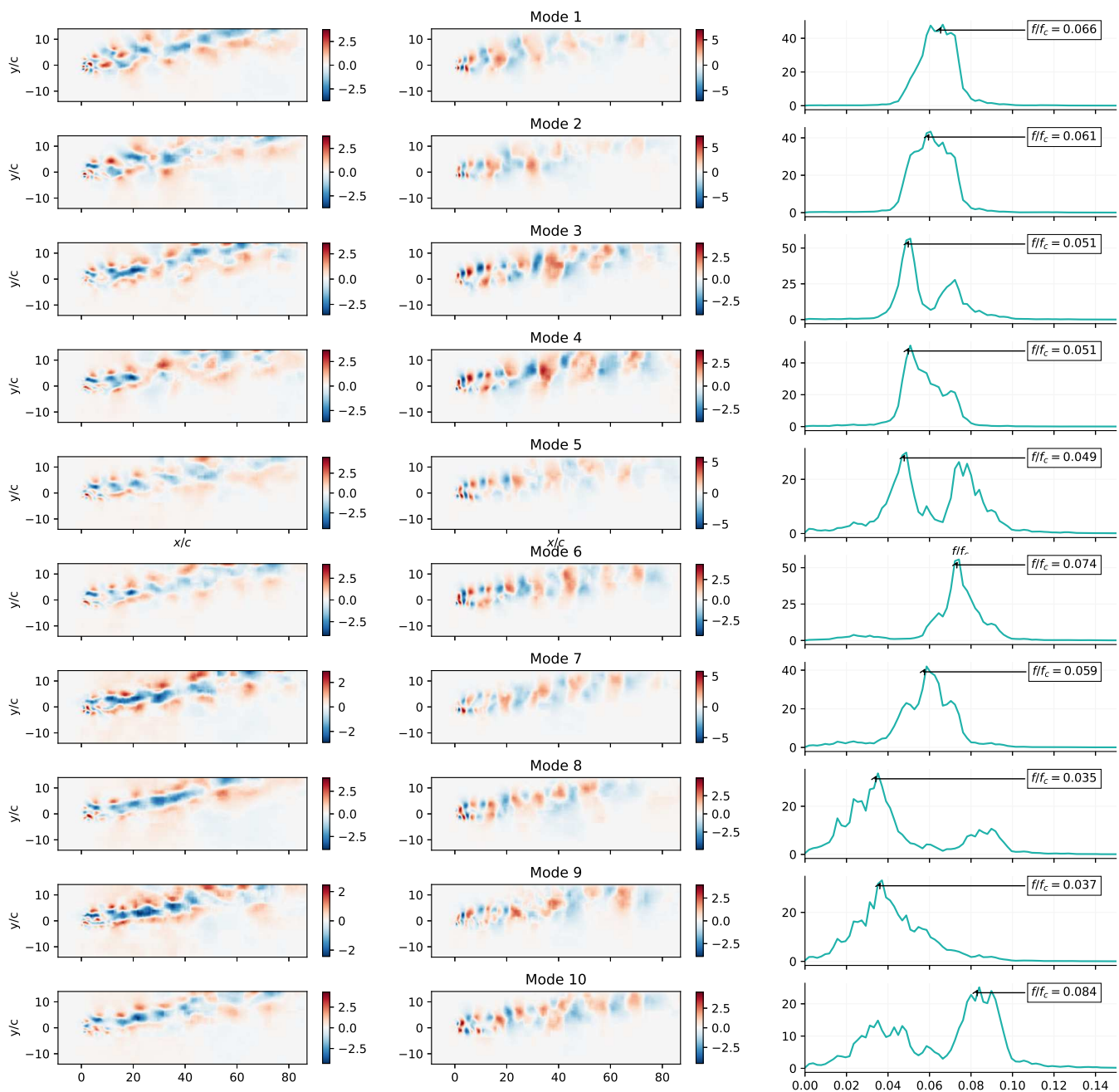


FIG. 4: Resulting  $\beta$ -VAE spatial modes for  $Re = 100$ ,  $\alpha = 80^\circ$  ranked according to their contribution to  $E_k$ . The first column contains  $u$  values for modes sampled  $\mathbf{r}_i$ . The second column shows the  $v$  values for the same inputs. The third column represents the frequency content of each individual mode ( $f_c = U_\infty/c$ ).

temporal dynamics of a low-order model of near-wall turbulence, showing that both approaches can reproduce the temporal dynamics of this system. Furthermore, the transformer has been used in the context of temporal predictions of turbulent flows in Ref. [31]. The three model architectures have been tuned to obtain the lowest mean-squared error over the validation data.

All three predictor models are trained to predict the next time step of a temporal sequence of previous latent-space  $\mathbf{r}_i$  vectors. Further details of the process and hyperparameter choice are detailed in the Methods section. Once trained, the models are used recursively to predict the next time steps. By predicting long time series, we can determine whether the model has been able to learn the system dynamics correctly. Figure 8(a) shows the true  $\mathbf{r}_i$  values for the test data and the corresponding  $\mathbf{p}_i$  predictions from each model. As expected for a chaotic dynamical

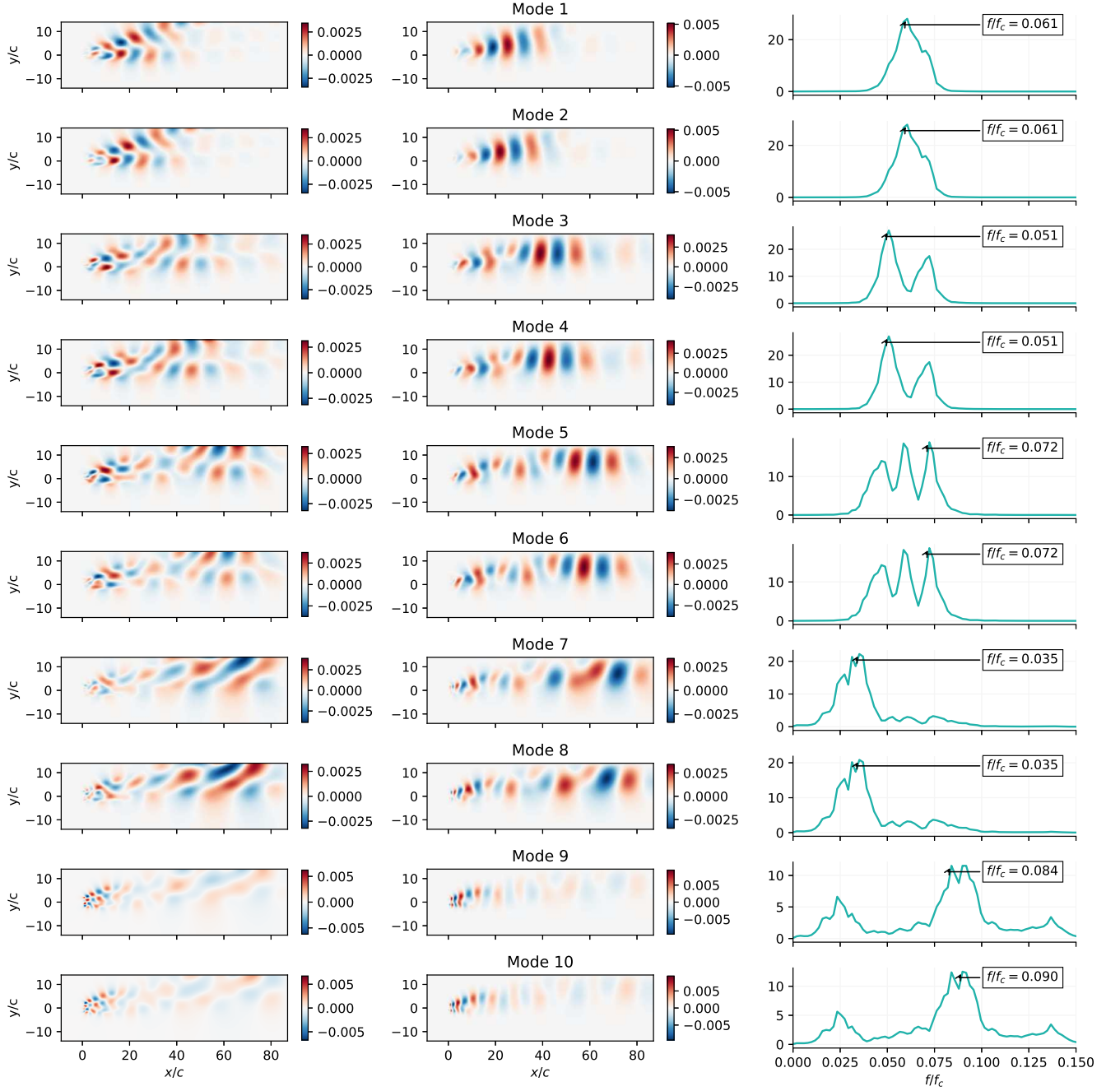


FIG. 5: POD spatial modes for  $Re = 100$ ,  $\alpha = 80^\circ$ . The first column contains  $u$  values for modes sampled  $r_i = 1$ . The second column shows the  $v$  values for the same inputs. The third column represents the frequency content of each individual mode ( $f_c = U_\infty/c$ ).

system, all predictor models diverge from the original trajectory after several time steps and appear to exhibit similar quantitative performance. To further evaluate the deviation error after several time steps, the ensemble average of the L2 error norm to the prediction horizon is defined as:

$$\varepsilon(\Delta t) = \left\langle \left( \sum_{i=0}^d (p_i(t) - r_i(t))^2 \right)^{1/2} \right\rangle_{\text{ensemble}}. \quad (4)$$

This quantity is shown in Figure 8(b) and the ensemble is computed over all the possible windows in the test data to

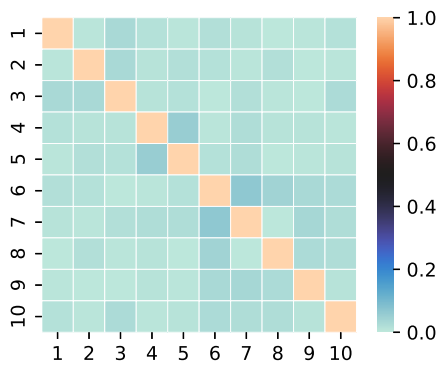


FIG. 6: Correlation matrix corresponding to the  $\beta$ -VAE mode coefficients for the case with  $Re = 100$ ,  $\alpha = 80^\circ$   $\det_{\mathbf{R}} = 0.982$ .

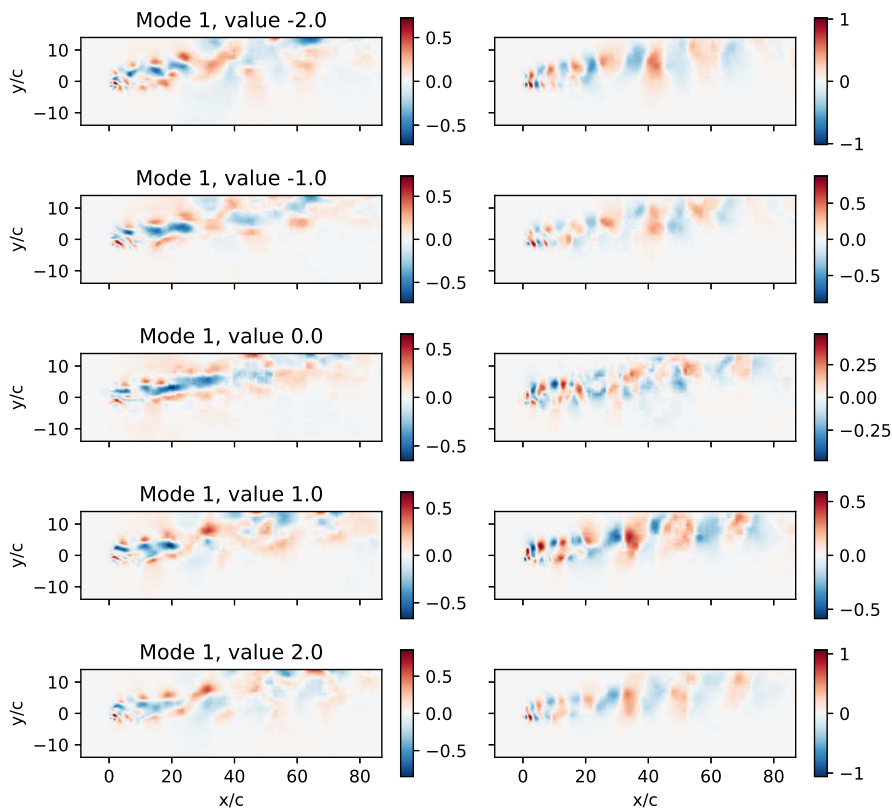


FIG. 7: Visualisation of the first  $\beta$ -VAE mode with different latent input values. The first column contains the streamwise-velocity component modes and the second one the crosswise-velocity component. Case with  $Re = 100$ ,  $\alpha = 80^\circ$

capture the average trend. This plot shows how the error  $\varepsilon(\Delta t)$  increases as the prediction horizon  $\Delta t$  gets longer. It can be seen that the error growth of the LSTM and KNF models is slower, which at first sight would suggest a better prediction by these models. However, since all predictions tend to diverge after several time steps, this result alone does not imply that the LSTM or KNF models would properly capture the system dynamics. Therefore, this aspect is further evaluated in terms of the dynamic behaviour of the system through the Poincaré-map analysis using the predictions for 1,024 additional time steps not seen during the training process.

The Poincaré map is constructed as the intersection of the latent vectors with the hyperplane  $r_1 = 0$  on the  $r_6 - r_{10}$  space with direction  $dr_1/dt > 0$ , using then a probability density function (PDF) to fit the resulting intersection points. These distributions are plotted for the true data and the model predictions in Figure 9. This figure shows the



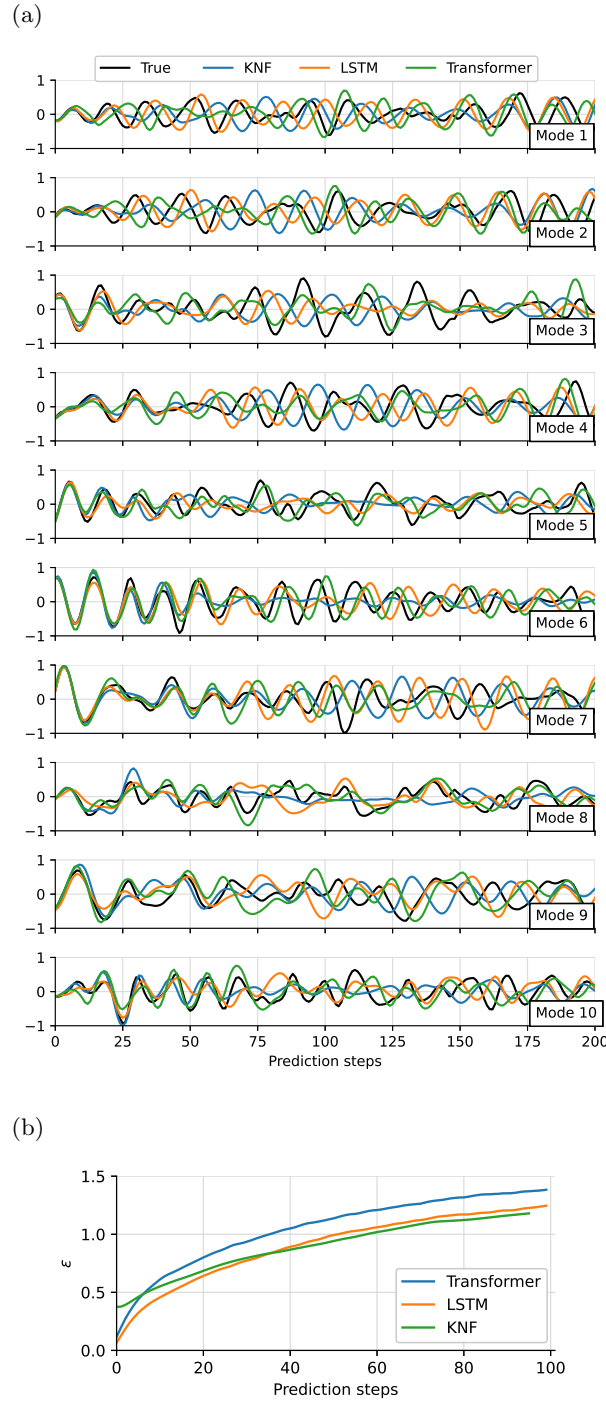


FIG. 8: (a) Reference values and predictions of latent-space modes by different models. (b) Average prediction error over the prediction horizon. This is shown for the case with  $Re = 100$ ,  $\alpha = 80^\circ$ .

correlation between the amplitudes of the  $r_5$  and  $r_9$  latent variables at the intersection. It can be seen from these figures that the LSTM and, to a lesser extent, the KNF models do not adequately reproduce the variability of this correlation. This result can be explained by the tendency of the LSTM model to converge towards a harmonic behaviour as the prediction progresses, which does not capture the variability in the evolution of the temporal coefficients that represent this chaotic flow. The transformer produces accurate predictions of the dynamics of the system using the patterns and correlations between the different  $r_i$  in the latent-space learned by the  $\beta$ -VAE. This comparison between models suggests that focusing only on instantaneous predictions may not be the correct approach to develop ROM models

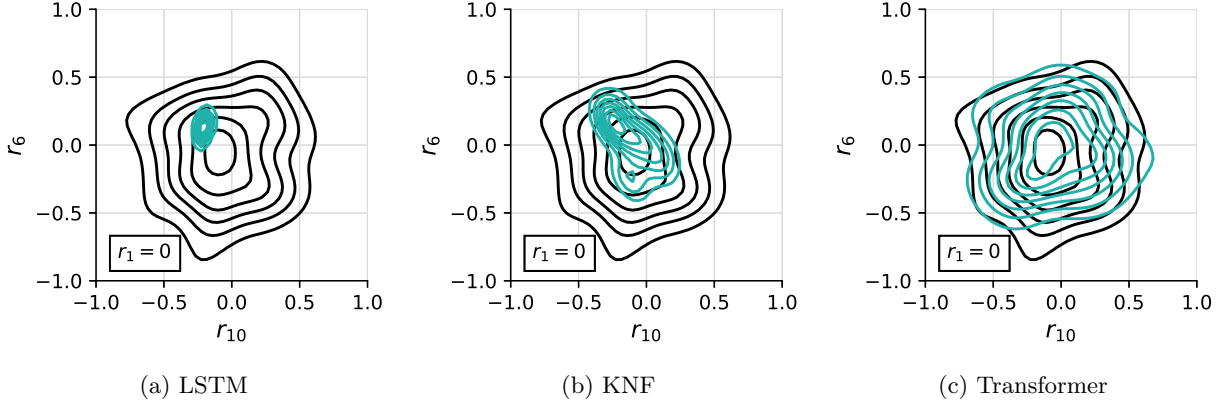


FIG. 9: Poincaré sections with plane  $r_0 = 0$  and  $dr_0/dt > 0$ . Black lines correspond to the original data and blue lines to the predicted data.

based on ML techniques.

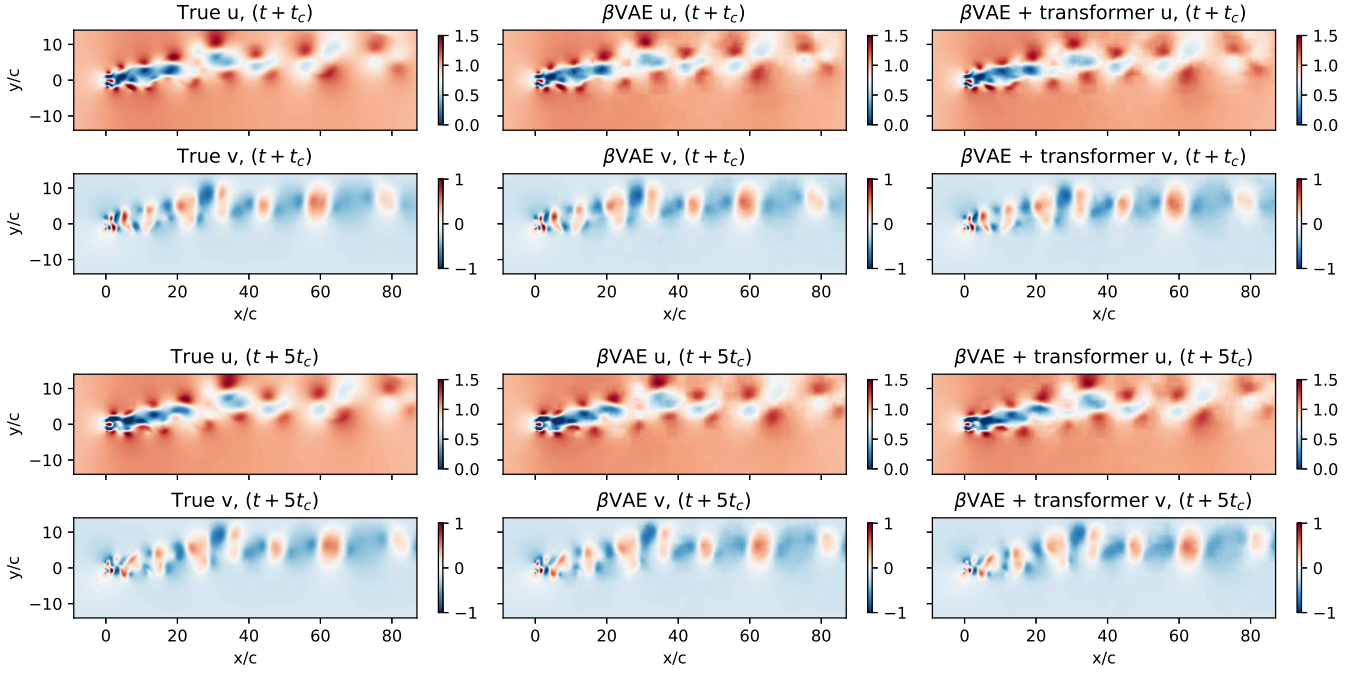


FIG. 10: True, reconstructed and predicted fields for  $u$  and  $v$  velocity components. Top two rows show the prediction of the next time step ( $t + t_c$ ), while the bottom rows show the prediction of the snapshot at  $t + 5t_c$  time step.

Using the latent vectors predicted with the transformer, we can develop a ROM of the flow in the latent-space that captures the underlying dynamics, as shown by the Poincaré maps, and then using these predicted  $r_i$  values the  $\beta$ -VAE decoder network can be used to project the predicted latent-space vector back into physical space, completing the flow field prediction model. The results of this prediction are shown in Figure 10. In the figure, the first column shows the actual  $t + n$  flow field in the dataset, the second column shows the same snapshot compressed into latent-space and decompressed by the  $\beta$ -VAE network, and the last column shows the field predicted by the ROM created using the  $\beta$ -VAE and transformer. The first two rows correspond to a prediction of the next time step, while the bottom two rows correspond to the result of the recurrent application of the transformer model to predict the next 5 time steps, being the time step equal to a one convective time  $t_c = c/U_\infty$ . The calculation of the reconstructed energy of the predicted fields for time steps  $t + t_c$  and  $t + 5t_c$  yields  $E_k$  values of 95.86% and 94.96%, respectively. These results support the quality of the reconstruction observed in Figure 10, even after several time steps equal to the convective

time, and confirm the robustness of the methodology proposed in this work.

## Discussion

This study presents and evaluates a ROM framework based on  $\beta$ -VAE architectures to produce robust non-linear latent-spaces, combined with the time-prediction model obtained by means of a transformer architecture. Using a two-dimensional viscous flow around two collinear flat plates in periodic and chaotic regimes, a first analysis of the  $\beta$ -VAE capabilities and the latent-spaces generated using these techniques is assessed and compared with the ROM obtained through POD modes. For the periodic case, it is observed that the same modal features are obtained, representing a vortex shedding with an equivalent number of energetic modes. For the chaotic case, the  $\beta$ -VAE learns a compact near-orthogonal latent-space that significantly improves the energy reconstruction obtained by the POD using ten modes,  $E_k = 95.3\%$  against  $E_k = 48.79\%$ . While the  $\beta$ -VAE ROM comprises 10 modes, a total of 100 POD modes would be required to match the result obtained by the  $\beta$ -VAE (in terms of flow reconstruction). The resulting modes from the  $\beta$ -VAE analysis exhibit temporal dynamics with shedding frequencies equivalent to those observed in the most energetic POD modes suggesting that the  $\beta$ -VAE is able to obtain non-linear modes that represent the most energetic or representative flow features.

The latent-space generated by the  $\beta$ -VAE is combined with a transformer architecture to predict the temporal dynamics. Its performance is compared against other models used in previous studies, such as LSTM or KNF. The results show that despite the fact that the prediction error is similar for all the methods, only the transformer can learn the correlations among the various temporal coefficients. Combining the  $\beta$ -VAE and the transformer models, we obtain a ROM model that can produce predictions with  $E_k$  equal to 95.86% and 94.96% at  $t+t_c$  and  $t+5t_c$ . This study constitutes a proof of concept of the capabilities of these novel ML techniques to generate compact and robust non-linear ROMs that can be employed to generate predictions in chaotic flows while capturing the most relevant flow features. The combination of various VAE and transformer architectures exhibits great potential for the future of ROM development in fluid mechanics, leveraging the inherent nonlinearities of these techniques.

## Methods

### $\beta$ -VAE implementation details

The variational autoencoder (VAE) described in Kingma and Welling [38] is one of the most common architectures used in generative models. In the basic autoencoder architecture, the input  $\mathbf{x}$  is directly encoded as a vector  $\mathbf{r}$  using the encoder  $\mathcal{E}$ ,  $\mathbf{r} = \mathcal{E}(\mathbf{x})$  in a lower-dimensional space of size  $d$ , which can be mapped back to the original space by the decoder  $\tilde{\mathbf{x}} = \mathcal{D}(\mathbf{r})$ , being  $\tilde{\mathbf{x}}$  the reconstructed output. A disadvantage of conventional autoencoders is the fact that there are no constraints imposed on the learned latent-space. The lack of constraints in the generated latent-space can lead to overfitting and poor generalisation performance, especially for high-dimensional input data. In contrast, in VAE architectures the encoder maps input data to a parameterised prior distribution, usually a Gaussian distribution, in the latent-space  $\boldsymbol{\mu}, \boldsymbol{\sigma} = \mathcal{E}(\mathbf{x})$ , where  $\boldsymbol{\mu}$  and  $\boldsymbol{\sigma}$  denote the mean and the standard deviation, respectively. The prior Gaussian distribution encourages the model to learn a compact and smooth representation of the input data. The distribution of the latent-space is then randomly sampled, and this sample is decoded back into the original space by the decoder  $\tilde{\mathbf{x}} = \mathcal{D}(\mathbf{s})$ , with  $\mathbf{s}$  following a distribution  $\mathbf{s} \sim N(\boldsymbol{\mu}, \boldsymbol{\sigma})$ . The architecture can therefore produce different outputs for the same input data, each sampled from the corresponding latent distribution. The encoder and decoder neural networks are trained by gradient descent and backpropagation, enabled by a re-parameterisation of the distribution sampling [38]. The training process for the VAE involves simultaneous training of the encoder and decoder networks with a compound loss function  $\mathcal{L}$ ,

$$\mathcal{L}(\mathbf{x}) = \underbrace{\frac{1}{N_t} \sum_{i=1}^{N_t} (\mathbf{x} - \tilde{\mathbf{x}})^2}_{\text{Reconstruction loss}} - \underbrace{\frac{1}{2} \sum_{i=1}^d (1 + \log(\sigma_i^2) - \mu_i^2 - \sigma_i^2)}_{\text{KL loss}}, \quad (5)$$

where  $N_t$  denotes the total number of points the in  $\mathbf{x}$ . The first term in the loss function is the reconstruction loss,  $\mathcal{L}_{rec}$ , which measures the model accuracy in reconstructing the input data from the reduced latent-space representation. The second term in the loss function is the Kullback–Leibler (KL) divergence loss [39],  $\mathcal{L}_{KL}$ , which measures the difference between the generated probability distribution and a prior probability distribution, typically Gaussian. The overall training goal is to optimise the model to produce accurate reconstructions while keeping the latent distributions close to a standard normal distribution.

The original VAE architecture was extended by Higgins et al. [40] to the  $\beta$ -variational autoencoder ( $\beta$ -VAE) architecture, which aims to promote disentangled representations in latent-space [18]. The  $\beta$ -VAE loss function, defined in equation (6), includes a scalar hyperparameter  $\beta \geq 0$  that modulates the trade-off between reconstruction accuracy and latent-space disentanglement. A higher value of  $\beta$  results in a more disentangled representation but may decrease reconstruction accuracy, whereas lower value of  $\beta$  may result in a more accurate reconstruction but a less disentangled latent-space. As a result, by incorporating the  $\beta$  parameter into the loss function, the  $\beta$ -VAE architecture can achieve a more interpretable and disentangled latent-space, which may improve the model generalisation ability.

$$\mathcal{L}(\mathbf{x}) = \mathcal{L}_{rec} - \frac{\beta}{2} \mathcal{L}_{KL}. \quad (6)$$

The  $\beta$ -VAE architecture is adapted from Ref. [20]. The encoder is used to generate the temporal modes for the latent-space representation using the mean vector for each time step  $\mathbf{r}_t = \boldsymbol{\mu}_t$ . The mean vectors are generated by applying the encoder  $\mathcal{E}$  to each input timestep:  $\boldsymbol{\mu}_t, \boldsymbol{\sigma}_t = \mathcal{E}(\mathbf{x}_t)$ . The spatial modes are reconstructed one by one:  $Y_i = \mathcal{D}(\mathbf{s}_i)$ . Here  $Y_i$  is the  $i^{th}$  spatial mode,  $\mathcal{D}$  is the decoder and  $\mathbf{s}_i$  is the vector that selects the mode to be reconstructed ( $\mathbf{s}_i = \delta_i^j = (0, \dots, 1, \dots, 0)$ ). The  $\beta$ -VAE architecture is sketched in Fig. 11.

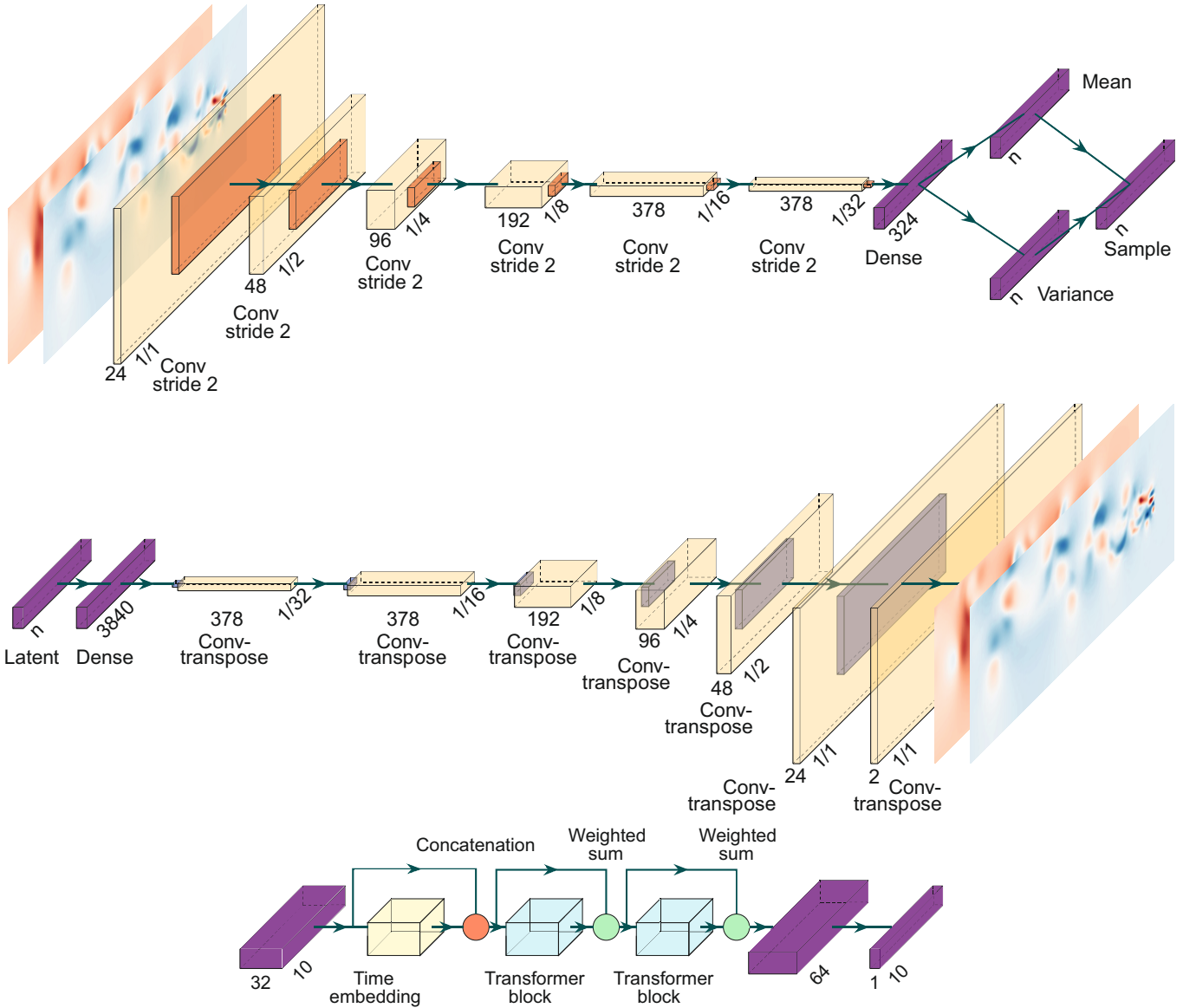


FIG. 11: Model architectures: (top)  $\beta$ -VAE encoder, (middle)  $\beta$ -VAE decoder and (bottom) transformer.

The nature of the data determines the choice of a convolutional neural network (CNN) to build the encoder, since the patterns in the flow can be better captured by convolutional layers that preserve the spatial relationships between points in the input. Figure 11 shows a representation of the model. In the encoder, we use six convolutional layers with a stride of two so that each layer halves the spatial dimension. The spatial reduction allows the subsequent layers to capture information at larger scales in the input flow data, which also has similarities to the multiple scales of the studied chaotic flow and can help to represent it. The number of filters in each layer progressively increases to preserve the information flow while reducing the spatial dimension. After the sixth convolutional layer, the spatial information is discarded, and a fully-connected layer is added to combine the information. Finally, two parallel layers with the same number of units as the latent-space dimension are used to output the mean and variance of the latent statistical distributions. During training, the distributions are sampled to generate inputs to the decoder network, while only the  $\boldsymbol{\mu}$  values are used to encode the time series used later by the predictor.

The decoder model is designed as an almost symmetric network to the encoder. Latent-space samples are fed into a fully-connected layer, and its output is reshaped to the same shape as the last convolutional layer in the encoder. Six transposed convolution layers are then used to increase the spatial dimension with decreasing filters. A final transposed convolution layer with two filters produces the two output channels. The chosen activation function is the exponential linear unit (ELU) [41] for all layers except the last, where the activation is linear.

### Proper orthogonal decomposition

In this section POD is employed as a reference to compare the resulting modes from the  $\beta$ -VAE latent-space with those obtained using this classical method. In particular, the snapshot method [42] has been used for the present study. Considering the streamwise and crosswise velocity components defined as  $U(\mathbf{x}, t)$  and  $V(\mathbf{x}, t)$ , respectively, being  $\mathbf{x} = (x, y)$  with  $x$  and  $y$  the streamwise and crosswise coordinates and  $t$  the time. We decompose the velocity components as:

$$U(\mathbf{x}, t) = \bar{U}(\mathbf{x}) + u(\mathbf{x}, t), \quad V(\mathbf{x}, t) = \bar{V}(\mathbf{x}) + v(\mathbf{x}, t) \quad (7)$$

where  $\bar{U}(\mathbf{x})$  and  $\bar{V}(\mathbf{x})$  are the streamwise and crosswise time-averaged velocity components and  $u(\mathbf{x}, t)$  and  $v(\mathbf{x}, t)$  are the streamwise and crosswise fluctuating velocity components. The fluctuating quantities can be approximated as a linear combination of basis functions  $\phi_i(\mathbf{x})$  as:

$$u(\mathbf{x}, t) \approx \sum_{i=1}^{N_m} a_i^u(t) \phi_i^u(\mathbf{x}), \quad v(\mathbf{x}, t) \approx \sum_{i=1}^{N_m} a_i^v(t) \phi_i^v(\mathbf{x}), \quad (8)$$

where  $a_i(t)$  are time-dependent coefficients and  $N_m$  is the number of basis functions used. Here we assume a number of images  $N_t$ , each one consisting of  $N_p$  grid points along the spatial domain  $\mathbf{x}$ , with  $N_t < N_p$ . Following the snapshot method [42], each image can be treated as an  $N_p$ -dimensional vector and the data can be arranged into an  $N_t \times N_p$  snapshot matrix:

$$\mathbf{u} = \begin{bmatrix} u(x_1, t_1) \cdots u(x_{N_p}, t_1) \\ \vdots \quad \ddots \quad \vdots \\ u(x_1, t_{N_t}) \cdots u(x_{N_p}, t_{N_t}) \end{bmatrix}; \quad \mathbf{v} = \begin{bmatrix} v(x_1, t_1) \cdots v(x_{N_p}, t_1) \\ \vdots \quad \ddots \quad \vdots \\ v(x_1, t_{N_t}) \cdots v(x_{N_p}, t_{N_t}) \end{bmatrix}. \quad (9)$$

Using the snapshot matrix, the two-point correlation matrix can be written as  $\mathbf{G} = \mathbf{u} \mathbf{u}^T + \mathbf{v} \mathbf{v}^T$ , where the superscript  $T$  refers to the matrix transpose. Solving the eigenvalue problem of  $\mathbf{G}$  returns the eigenvalues  $\lambda_i$  and the left and right eigenvector matrices. The left and right eigenvector matrices are respectively the matrix  $\boldsymbol{\Psi}$  containing in its columns the temporal modes  $\mathbf{a}_i$  (which are orthonormal vectors of length  $N_t$  and unitary norm) and its inverse (i.e. its transpose). Note that the columns of  $\boldsymbol{\Psi}$  form a basis of rank  $N_t$  and that the eigenvalues  $\lambda_i$  are representative of the energy contribution of each mode. The orthonormal spatial modes  $\phi_n(\mathbf{x})$  can then easily be computed as  $\boldsymbol{\Sigma}_u \boldsymbol{\phi}_u = \boldsymbol{\Psi}^T \mathbf{u}$  and  $\boldsymbol{\Sigma}_v \boldsymbol{\phi}_v = \boldsymbol{\Psi}^T \mathbf{v}$ , where  $\boldsymbol{\Sigma}_u$  and  $\boldsymbol{\Sigma}_v$  are diagonal matrices which, in each  $i^{th}$  diagonal element, contain the streamwise and wall-normal Reynolds-stress contributions of the  $i^{th}$  mode.

### Time-series prediction models

The  $\beta$ -VAE encoder network is used to generate the entire dataset latent-space time series. The last 1024 time steps are then used as test data and the rest is used for training. The transformer model predicts the next latent-space

vector in a sequence of latent vectors generated by the  $\beta$ -VAE. The input to the transformer at each time step is a sequence of 32 time steps, and the output is the prediction of the next time step for the latent vector in the sequence. The transformer is trained to minimise the difference between the prediction of the next time step and the true data using a mean-squared-error loss function.

A time-embedding vector [43] is added to each input latent-space vector to incorporate temporal information into the model. The time-embedding vector represents the time step at which the latent vector was generated, allowing the model to distinguish between latent vectors generated at different time steps and to capture the temporal dynamics of the physical system. The time embedding is a vector which is learned together with the other parameters of the transformer model during training. It is randomly initialised at the start of training and updated during backpropagation in the same way as the other parameters of the model.

The transformer model comprises a set of encoder and decoder layers, each consisting of a multi-head attention block and a feed-forward neural network. The attention blocks allow the model to weight the importance of different parts of the input sequence when making predictions [44], while the feed-forward network allows it to learn complex non-linear relationships between the input and output sequences. Two transformer blocks are concatenated with skip connections around them to enhance gradient propagation towards the input during the backpropagation phase of training [45]. After the transformer blocks, feed-forward layers learn the complex non-linear relationships in the transformer output and form the final latent-space vector prediction. The architecture is illustrated in Figure 11. To tune the number of blocks, layers and neurons per layer among other hyperparameters, the KerasTuner framework [46] was employed using a Bayesian-optimisation algorithm to evaluate different models, using the validation error as the reference metric. The LSTM model architecture was also tuned searching the lowest prediction error in the test data. The resulting architecture includes two layers of 128 LSTM elements, followed by a fully-connected layer of 128 neurons and a final output layer matching the latent-space size. The input for the LSTM includes the previous 16 time steps, the same as for the transformer model. The KNF-model implementation is based in the code from Ref. [22]. After the hyperparameter tuning, the number of previous time steps used to predict is 5, and the maximum order of the functions for construction of the forcing term is 3 for polynomial functions and 4 for trigonometric functions.

### Training setup

The TensorFlow 2.10 deep-learning framework [47] was used to implement the models and the training pipeline. An NVIDIA A100-SXM GPU was used to train the models within the Google Colaboratory framework. Training the  $\beta$ -VAE model took about 1 hour while training the transformer model took only a few minutes. The  $\beta$ -VAE model is trained using the Adam algorithm [48] with a lookahead mechanism [49] and gradient clipping of 0.5 for stability requirements [50]. The synchronisation period for the lookahead mechanism is 6, and the slow step size is 0.4. The learning rate is variable, starting at  $5 \times 10^{-4}$  and decreasing with a piecewise constant decay to  $3 \times 10^{-5}$ . The model is trained over 1000 epochs. The encoder network has  $3.61 \times 10^6$  trainable parameters, while the decoder network has  $3.48 \times 10^6$ . The entire dataset is used for training the  $\beta$ -VAE model. The resulting temporal dynamics from the  $\beta$ -VAE are then used to train a transformer architecture using the NovoGrad algorithm [51] with a gradient-clipping value of 0.5 for stability reasons. The learning rate was set to 0.001, and the model was trained for 256 epochs. The number of trainable parameters for this model is  $2.41 \times 10^5$ . In this case, the last 1024 time steps are not used during training and are used to test the prediction models.

### Dataset description and pre-processing

The source data set is an incompressible, two-dimensional, viscous flow over two collinear flat plates. Numerical simulation is used to solve the governing Navier–Stokes equations for this flow using an immersed-boundary projection method (IBPM) [52, 53]. The two plates have a chord length  $c$  and are separated by a gap of the same size. The free stream velocity is  $U_\infty$ , and the Reynolds number,  $Re$ , is defined based on the free stream velocity and single-plate chord length.

The simulations are performed on a series of nested grids of increasing size and decreasing resolution. The finest resolution for the simulation has a grid spacing of  $\Delta x = \Delta y = 0.02c$ , and the total computational domain has dimensions of  $96c \times 28c$ , with the upstream boundary at  $x = -9c$ . The dataset generation and its characteristics are described in more detail in Ref. [54]. The time step in the dataset (downsampled from the simulations) was chosen to be equal to the convective time  $\Delta t = c/U_\infty = t_c$ , which is sufficient to resolve the dynamics of coherent vortical structures in the wake.

The dataset employed for this study is downsampled from the original mesh to a spatial resolution of  $300 \times 98$  with a uniform grid spacing, to reduce the GPU requirements for training. The fluctuation components of the streamwise  $u$  and crosswise  $v$  velocity were stacked as separate channels in the dataset. The values in the dataset were standardised by subtracting the pixel-wise average and dividing by the standard deviation for each component over the entire

dataset. The resulting dataset size was reduced to 1.8 GB and fully loaded into memory during training. This approach allowed the training process to be efficient while still capturing the essential features of the fluid flow.

#### Data availability

The dataset will be made publicly available after publication.

#### Code availability

The codes will be made publicly available after publication.

#### Acknowledgements

The authors would like to thank to Dr. Hamidreza Eivazi and Mr. Samuel Molina for their technical assistance in the first part of the study and Dr. Steve Brunton for his insightful suggestions. Some of the deep-learning models were trained by means of resources provided by the National Academic Infrastructure for Supercomputing in Sweden (NAISS). RV acknowledges the financial support from ERC grant no. ‘2021-CoG-101043998, DEEPCONTROL’. Views and opinions expressed are however those of the author(s) only and do not necessarily reflect those of the European Union or the European Research Council. Neither the European Union nor the granting authority can be held responsible for them.

#### Author contributions

ASR: Methodology, Software, Validation, Investigation, Data Curation, Writing - Original Draft, Writing - Review & Editing, Visualization. CSV: Methodology, Software, Validation, Investigation, Data Curation, Writing - Original Draft, Writing - Review & Editing, Visualization. MAG: Methodology, Writing - Review & Editing. YW: Methodology, Software, Validation, Writing - Review & Editing. AA: Data generation. SD: Data generation, Writing - Original Draft, Writing - Review & Editing. RV: Ideation, Methodology, Writing - Review & Editing, Resources, Funding acquisition.

#### Competing interests

The authors declare that they have no competing interests.

#### References

- 
- [1] J. Jiménez, Coherent structures in wall-bounded turbulence, *Journal of Fluid Mechanics* **842**, P1 (2018).
  - [2] K. Taira, S. L. Brunton, S. T. Dawson, C. W. Rowley, T. Colonius, B. J. McKeon, O. T. Schmidt, S. Gordeyev, V. Theofilis, and L. S. Ukeiley, Modal analysis of fluid flows: An overview, *Aiaa Journal* **55**, 4013 (2017).
  - [3] K. Taira, M. S. Hemati, S. L. Brunton, Y. Sun, K. Duraisamy, S. Bagheri, S. T. Dawson, and C.-A. Yeh, Modal analysis of fluid flows: Applications and outlook, *AIAA journal* **58**, 998 (2020).
  - [4] C. W. Rowley and S. T. Dawson, Model reduction for flow analysis and control, *Annual Review of Fluid Mechanics* **49**, 387 (2017).
  - [5] D. J. Lucia, P. S. Beran, and W. A. Silva, Reduced-order modeling: new approaches for computational physics, *Progress in Aerospace Sciences* **40**, 51 (2004).
  - [6] S. L. Brunton, B. R. Noack, and P. Koumoutsakos, Machine learning for fluid mechanics, *Annu. Rev. Fluid Mech.* **52**, 477 (2020).
  - [7] P. J. Schmid, Dynamic mode decomposition of numerical and experimental data, *Journal of fluid mechanics* **656**, 5 (2010).
  - [8] M. Sieber, C. O. Paschereit, and K. Oberleithner, Spectral proper orthogonal decomposition, *Journal of Fluid Mechanics* **792**, 798 (2016).
  - [9] S. Le Clainche and J. M. Vega, Higher order dynamic mode decomposition, *SIAM Journal on Applied Dynamical Systems* **16**, 882 (2017).
  - [10] L. I. Abreu, A. V. Cavalieri, P. Schlatter, R. Vinuesa, and D. S. Henningson, Spectral proper orthogonal decomposition and resolvent analysis of near-wall coherent structures in turbulent pipe flows, *Journal of Fluid Mechanics* **900**, A11 (2020).

- [11] G. Berkooz, P. Holmes, and J. L. Lumley, The proper orthogonal decomposition in the analysis of turbulent flows, *Annual review of fluid mechanics* **25**, 539 (1993).
- [12] H. Eivazi, H. Veisi, M. H. Naderi, and V. Esfahanian, Deep neural networks for nonlinear model order reduction of unsteady flows, *Physics of Fluids* **32**, 105104 (2020).
- [13] S. Hijazi, G. Stabile, A. Mola, and G. Rozza, Data-driven pod-galerkin reduced order model for turbulent flows, *Journal of Computational Physics* **416**, 109513 (2020).
- [14] T. Murata, K. Fukami, and K. Fukagata, Nonlinear mode decomposition with convolutional neural networks for fluid dynamics, *Journal of Fluid Mechanics* **882**, A13 (2020).
- [15] R. Vinuesa and S. L. Brunton, Enhancing computational fluid dynamics with machine learning, *Nature Computational Science* **2**, 358 (2022).
- [16] K. Fukami, T. Nakamura, and K. Fukagata, Convolutional neural network based hierarchical autoencoder for nonlinear mode decomposition of fluid field data, *Physics of Fluids* **32**, 095110 (2020).
- [17] P. A. Srinivasan, L. Guastoni, H. Azizpour, P. Schlatter, and R. Vinuesa, Predictions of turbulent shear flows using deep neural networks, *Physical Review Fluids* **4**, 054603 (2019).
- [18] C. P. Burgess, I. Higgins, A. Pal, L. Matthey, N. Watters, G. Desjardins, and A. Lerchner, Understanding disentangling in  $\beta$ -VAE, *arXiv preprint arXiv:1804.03599* (2018).
- [19] I. Higgins, L. Matthey, A. Pal, C. Burgess, X. Glorot, M. Botvinick, S. Mohamed, and A. Lerchner,  $\beta$ -vae: Learning basic visual concepts with a constrained variational framework, in *International conference on learning representations* (2017).
- [20] H. Eivazi, S. Le Clainche, S. Hoyas, and R. Vinuesa, Towards extraction of orthogonal and parsimonious non-linear modes from turbulent flows, *Expert Systems with Applications* **202**, 117038 (2022).
- [21] T. Nakamura, K. Fukami, K. Hasegawa, Y. Nabae, and K. Fukagata, Convolutional neural network and long short-term memory based reduced order surrogate for minimal turbulent channel flow, *Physics of Fluids* **33**, 025116 (2021).
- [22] H. Eivazi, L. Guastoni, P. Schlatter, H. Azizpour, and R. Vinuesa, Recurrent neural networks and Koopman-based frameworks for temporal predictions in a low-order model of turbulence, *International Journal of Heat and Fluid Flow* **90**, 108816 (2021).
- [23] A. Vaswani, N. Shazeer, N. Parmar, J. Uszkoreit, L. Jones, A. N. Gomez, L. u. Kaiser, and I. Polosukhin, Attention is all you need, in *Advances in Neural Information Processing Systems*, Vol. 30, edited by I. Guyon, U. V. Luxburg, S. Bengio, H. Wallach, R. Fergus, S. Vishwanathan, and R. Garnett (Curran Associates, Inc., 2017).
- [24] S. Yang, Y. Wang, and X. Chu, A survey of deep learning techniques for neural machine translation, *arXiv preprint arXiv:2002.07526* (2020).
- [25] T. Brown, B. Mann, N. Ryder, M. Subbiah, J. D. Kaplan, P. Dhariwal, A. Neelakantan, P. Shyam, G. Sastry, A. Askell, et al., Language models are few-shot learners, *Advances in neural information processing systems* **33**, 1877 (2020).
- [26] S. Khan, M. Naseer, M. Hayat, S. W. Zamir, F. S. Khan, and M. Shah, Transformers in vision: A survey, *ACM computing surveys (CSUR)* **54**, 1 (2022).
- [27] S. He, W. Liao, H. R. Tavakoli, M. Yang, B. Rosenhahn, and N. Pugeault, Image captioning through image transformer, in *Proceedings of the Asian Conference on Computer Vision (ACCV)* (2020).
- [28] Y. Gong, Y.-A. Chung, and J. Glass, Ast: Audio spectrogram transformer, *arXiv preprint arXiv:2104.01778* (2021).
- [29] A. Prakash, K. Chitta, and A. Geiger, Multi-modal fusion transformer for end-to-end autonomous driving, in *Proceedings of the IEEE/CVF Conference on Computer Vision and Pattern Recognition* (2021) pp. 7077–7087.
- [30] N. Geneva and N. Zabarar, Transformers for modeling physical systems, *Neural Networks* **146**, 272 (2022).
- [31] M. Z. Yousif, M. Zhang, L. Yu, R. Vinuesa, and H. Lim, A transformer-based synthetic-inflow generator for spatially developing turbulent boundary layers, *Journal of Fluid Mechanics* **957**, A6 (2023).
- [32] G. Borrelli, L. Guastoni, H. Eivazi, P. Schlatter, and R. Vinuesa, Predicting the temporal dynamics of turbulent channels through deep learning, *International Journal of Heat and Fluid Flow* **96**, 109010 (2022).
- [33] Y. Zhou and M. M. Alam, Wake of two interacting circular cylinders: A review, *International Journal of Heat and Fluid Flow* **62**, 510 (2016).
- [34] N. Deng, B. R. Noack, M. Morzyński, and L. R. Pastur, Low-order model for successive bifurcations of the fluidic pinball, *Journal of fluid mechanics* **884**, A37 (2020).
- [35] C. Ren, L. Cheng, C. Xiong, F. Tong, and T. Chen, Bistabilities in two parallel kármán wakes, *Journal of Fluid Mechanics* **929**, A5 (2021).
- [36] M. Khodkar and P. Hassanzadeh, A data-driven, physics-informed framework for forecasting the spatiotemporal evolution of chaotic dynamics with nonlinearities modeled as exogenous forcings, *Journal of Computational Physics* **440**, 110412 (2021).
- [37] S. Hochreiter and J. Schmidhuber, Long Short-Term Memory, *Neural Computation* **9**, 1735 (1997), <https://direct.mit.edu/neco/article-pdf/9/8/1735/813796/neco.1997.9.8.1735.pdf>.
- [38] D. P. Kingma and M. Welling, Auto-encoding variational bayes, *arXiv preprint arXiv:1312.6114* (2013).
- [39] S. Kullback and R. A. Leibler, On information and sufficiency, *The Annals of Mathematical Statistics* **22**, 79 (1951).
- [40] I. Higgins, L. Matthey, A. Pal, C. Burgess, X. Glorot, M. Botvinick, S. Mohamed, and A. Lerchner, beta-VAE: Learning basic visual concepts with a constrained variational framework, in *International Conference on Learning Representations* (2017).
- [41] D.-A. Clevert, T. Unterthiner, and S. Hochreiter, Fast and accurate deep network learning by exponential linear units (elus), *arXiv preprint arXiv:1511.07289* (2015).
- [42] L. Sirovich, Turbulence and the dynamics of coherent structures. i. coherent structures, *Quarterly of applied mathematics* **45**, 561 (1987).



- [43] S. M. Kazemi, R. Goel, S. Eghbali, J. Ramanan, J. Sahota, S. Thakur, S. Wu, C. Smyth, P. Poupart, and M. Brubaker, Time2vec: Learning a vector representation of time, arXiv preprint arXiv:1907.05321 (2019).
- [44] D. Bahdanau, K. Cho, and Y. Bengio, Neural machine translation by jointly learning to align and translate, arXiv preprint arXiv:1409.0473 (2014).
- [45] K. He, X. Zhang, S. Ren, and J. Sun, Deep residual learning for image recognition, in *Proceedings of the IEEE conference on computer vision and pattern recognition* (2016) pp. 770–778.
- [46] T. O’Malley, E. Bursztein, J. Long, F. Chollet, H. Jin, L. Invernizzi, et al., Kerastuner, <https://github.com/keras-team/keras-tuner> (2019).
- [47] M. Abadi, A. Agarwal, P. Barham, E. Brevdo, Z. Chen, C. Citro, G. S. Corrado, A. Davis, J. Dean, M. Devin, S. Ghemawat, I. Goodfellow, A. Harp, G. Irving, M. Isard, Y. Jia, R. Jozefowicz, L. Kaiser, M. Kudlur, J. Levenberg, D. Mané, R. Monga, S. Moore, D. Murray, C. Olah, M. Schuster, J. Shlens, B. Steiner, I. Sutskever, K. Talwar, P. Tucker, V. Vanhoucke, V. Vasudevan, F. Viégas, O. Vinyals, P. Warden, M. Wattenberg, M. Wicke, Y. Yu, and X. Zheng, TensorFlow: Large-scale machine learning on heterogeneous systems (2015), software available from tensorflow.org.
- [48] D. Kingma and J. Ba, Adam: A method for stochastic optimization, *International Conference on Learning Representations* (2014).
- [49] M. Zhang, J. Lucas, J. Ba, and G. E. Hinton, Lookahead optimizer: k steps forward, 1 step back, *Advances in neural information processing systems* **32** (2019).
- [50] R. Pascanu, T. Mikolov, and Y. Bengio, On the difficulty of training recurrent neural networks, in *International conference on machine learning* (Pmlr, 2013) pp. 1310–1318.
- [51] B. Ginsburg, P. Castonguay, O. Hrinchuk, O. Kuchaiev, V. Lavrukhin, R. Leary, J. Li, H. Nguyen, Y. Zhang, and J. M. Cohen, Stochastic gradient methods with layer-wise adaptive moments for training of deep networks, arXiv preprint arXiv:1905.11286 (2019).
- [52] K. Taira and T. Colonius, The immersed boundary method: a projection approach, *Journal of Computational Physics* **225**, 2118 (2007).
- [53] T. Colonius and K. Taira, A fast immersed boundary method using a nullspace approach and multi-domain far-field boundary conditions, *Computer Methods in Applied Mechanics and Engineering* **197**, 2131 (2008).
- [54] K. J. Asztalos, A. Almashjary, and S. Dawson, Galerkin spectral estimation of vortex-dominated wake flows, arXiv preprint arXiv:2302.06412 (2023).